

Radiative GRMHD simulations of accretion and outflow in non-magnetized neutron stars and ultraluminous X-ray sources

David Abarca,¹★ Włodek Kluźniak,¹ and Aleksander Sądowski²

¹*Nicolaus Copernicus Astronomical Center, Warsaw, Poland*

²*Akuna Capital, 585 Massachusetts Avenue, Cambridge, MA 02139*

Accepted XXX. Received YYY; in original form ZZZ

ABSTRACT

We run two GRMHD simulations of super-Eddington accretion disks around a black hole and a non-magnetized, non-rotating neutron star. The neutron star was modeled using a reflective inner boundary condition. We observe the formation of a transition layer in the inner region of the disk in the neutron star simulation which leads to a larger mass outflow rate and a lower radiative luminosity over the black hole case. Sphereization of the flow leads to an observable luminosity at infinity around the Eddington value when viewed from all directions for the neutron star case, contrasting to the black hole case where collimation of the emission leads to observable luminosities about an order of magnitude higher when observed along the disk axis. We find the outflow to be optically thick to scattering, which would lead to the obscuring of any neutron star pulsations observed in corresponding ULXs.

Key words: accretion, accretion discs – stars: neutron – (magnetohydrodynamics) MHD

1 INTRODUCTION

The transfer of matter with angular momentum onto a compact object occurs via an accretion disk through which mass and angular momentum are transported in opposite directions through viscous processes (Shakura & Sunyaev 1973). The viscous process is now believed to be magnetic turbulence induced by the magnetorotational instability (Balbus & Hawley 1991).

One particular class of accreting objects which has gained interest in recent years are ultraluminous X-ray sources (ULXs). These are X-ray bright objects observed outside the centers of galaxies with luminosities from $10^{39} \sim 10^{41}$ ergs s⁻¹. The first explanations for such bright X-ray objects favored the elusive intermediate mass black holes radiating at or below the Eddington luminosity (Colbert & Mushotzky 1999). Up until the discovery of ULXs, the most luminous stellar-mass, persistent X-ray source was known to be Sco X-1, a neutron star radiating at its Eddington limit at around 10^{38} erg s⁻¹ (Shklovsky 1967; Bradshaw et al. 1999). Currently, the leading explanation for ULXs is beamed emission from accretion in an X-ray binary (King et al. 2001), implying that or super-Eddington accretion is responsible for the large observed luminosities. In particu-

lar, a set of three such objects were observed which reveal X-ray pulsations with a period on the order of one second (Bachetti et al. 2014; Fürst et al. 2016; Israel et al. 2017a,b) excluding black holes as the accreting objects in these three sources. It can now be said with some certainty that a large fraction of ULXs are accreting neutron stars (Kluźniak & Lasota 2015; King et al. 2017; Wiktorowicz et al. 2017; Pintore et al. 2017). There have been a wide range of proposed values for the strength of the magnetic field from relatively low ($B < 10^9$ G) (Kluźniak & Lasota 2015), to moderate (10^{10} G $\lesssim B \lesssim 10^{13}$ G) (King et al. 2017; Walton et al. 2018), to high ($B > 10^{13}$ G), magnetar-like fields (Ekşi et al. 2015; Mushtukov et al. 2015b).

Accretion onto a neutron star (NS) is more complicated than accretion onto a black hole. Neutron stars have no event horizon. They have a surface layer and outer crust which can reach densities of up to 10^{11} g/cm³ at its base, where it is composed of fully ionized neutron rich nuclei. At larger radii, and lower densities ($\sim 10^7$ g cm⁻³) the composition of the nuclei becomes less neutron rich. Below 10^4 g cm⁻³, the nuclei are no longer fully ionized. Finally, near the surface, the outer crust is composed mainly of crystalized iron atoms reaching down to 10 g cm⁻³ (Chamel & Haensel 2008).

Gas accreting onto these outer layers is expected to slow down and release some of its kinetic energy (Syunyaev & Shakura 1986; Kluźniak & Wilson 1991; Narayan & Yi 1995;

★ E-mail: dabarca@camk.edu.pl (DA)

Narayan et al. 1997; Inogamov & Sunyaev 1999; Sibgatullin & Sunyaev 2000; Popham & Sunyaev 2001; Mukhopadhyay & Fang 2002) as it spins up the star (Kluźniak & Wagoner 1985). This energy can be converted into radiation (normally X-rays) or transferred to the outflowing gas. Additionally, many neutron stars have strong magnetic fields, some of which can be strong enough to channel the accreting gas into dense accretion columns, depositing gas at the magnetic poles, forming hot spots at low accretion rates, $\lesssim 10^{17} \text{ g s}^{-1}$. Misalignment of the magnetic poles with the rotation axis causes the hot spots to rotate resulting observationally in X-ray (accretion powered) pulsars. At high accretion rates ($10^{17} \sim 10^{19} \text{ g s}^{-1}$), the gas is expected to experience a radiation shock and to form an accretion column above the neutron star surface through which gas sinks slowly through a dense radiation field to eventually settle on the NS surface (Basko & Sunyaev 1976; Mushtukov et al. 2015a,b; Revnivtsev & Mereghetti 2015). As the accretion rate increases, the accretion column starts to widen and spread over a surface roughly corresponding to the surface of the magnetosphere. Emission from the central regions and through the sides of the inner part of the accretion column can interact with the outer parts of the accretion column producing complicated pulse profiles (Mushtukov et al. 2018).

At even higher accretion rates ($\gtrsim 10^{19} \text{ g s}^{-1}$), in the context of ULXs, the accretion column spreads into an accretion curtain, a geometrically extended surface corresponding to an optically thick layer completely surrounding the pulsar magnetosphere which reprocesses all of the radiation generated near the neutron star surface strongly smoothing the pulse profile (Mushtukov et al. 2017). Observationally, in pulsating and non-pulsating sources, this manifests as a double black body with hot ($>1\text{keV}$) and cold ($<0.7 \text{ keV}$) components corresponding to the thermal emission from the accretion enveloping the magnetosphere, and thermal emission from the accretion disk truncated at the magnetosphere, respectively (Koliopanos et al. 2017).

Here, using numerical simulations, we try to see if non-pulsating ULXs can be explained by super-Eddington accretion onto neutron stars. We ignore the effects of a stellar magnetic field, (for an accretion rate of ten times the Eddington limit and a magnetic moment of $\mu < 10^{27} \text{ G cm}^3$ a simple calculation of the Alfvén radius shows the effects of the magnetic field are confined close to the neutron star surface), and consider only the effects of a hard surface. We use a general relativistic radiation magnetohydrodynamic (GR-MHD) code KORAL to capture the most relevant physical processes.

1.1 Neutron star related accretion simulations

In this section we mention some simulations that are related to neutron star accretion. The X-ray spectra from spherical accretion onto high and low mass neutron stars was computed from coupled hydrodynamic radiation transfer calculations, which were shown to yield results which differ strongly from a black body (Alme & Wilson 1973). Dhang et al. (2016) performed hydrodynamic simulations of spherical accretion onto a hard surface in one and two dimensions. The hard surface was modeled in two ways, with a reflective, and a ‘leaky’ boundary condition, the latter being where mass is allowed to cross the inner boundary at a fixed

subsonic speed to model efficient cooling. This is important because not all works include a hard surface. More complicated Bondi-Hoyle (El Mellah & Casse 2015) and magnetic Bondi-Hoyle (Toropina et al. 2012) simulations have been performed, but they are without a hard inner boundary.

A 1.5D coupled radiative transfer and hydrodynamics calculation was performed by Kluźniak & Wilson (1991) which simulated the boundary layer between the neutron star and the accretion disk. The boundary layer was simulated by introducing an optically thin stream of plasma inside the innermost stable circular orbit (ISCO), where the infall velocity quickly becomes supersonic. The plasma decelerates in the upper layers of the boundary layer on the neutron star surface resulting in the creation of hard X-rays. Because velocities in the accretion gap are supersonic, such a calculation is valid without considering the contribution of the accretion disk.

A further work of interest is Kawashima et al. (2016) who performed radiation hydrodynamic simulations of the accretion column of a super-Eddington accretion neutron star using flux-limited diffusion, where the radiative flux follows the gradient of radiative energy density. They found sub-Eddington luminosities along the optically thick accretion column but super-Eddington luminosity when viewed from the sides, in agreement with Basko & Sunyaev (1976).

Romanova et al. (2012) have performed global MHD simulations of MRI-driven accretion onto magnetized stars. A number of interesting results are presented on the interaction between the stellar magnetic field and the accretion disk, however, the lack of strong gravity or radiation hydrodynamics means that the results do not accurately describe accretion onto neutron stars at large accretion rates.

Parfrey & Tchekhovskoy (2017) used an innovative method to run GRMHD simulations of accretion onto rotating magnetized neutron stars to model accreting millisecond pulsars. Their method interpolates between the normal GRMHD flow and the force-free magnetosphere. At the lowest magnetizations of the neutron star, they show that the magnetic field is crushed by the accretion flow, and accretion proceeds normally. Due to the lack of radiation, their simulations are scale-free. When scaling their system to the mildly super-Eddington accretion flow that we describe in this work, we find that indeed the magnetic field would be crushed at a magnetic moment of $\mu = 10^{26} \text{ G cm}^3$, even when rotating at millisecond periods.

Takahashi & Ohsuga (2017) have published the first global 2.5D GRRMHD simulations of accretion onto a neutron star and their work represents the state-of-the-art on the subject. They simulate super-Eddington accretion onto a magnetized neutron star with the radial flux and velocity set to zero at the inner boundary, as a means to model a neutron star ULX system. They report luminosities of about an order of magnitude above the Eddington limit with a significant amount of beaming which accurately describes a non-pulsating ULX source. In their simulation, the magnetic field is strong enough to truncate the disk leading to accretion along magnetic field lines. They observe some matter piling up at the inner boundary due to the inner boundary condition, but do not run the simulation for long duration, ($t_{\text{max}} = 15,000t_g$), and so it is hard to say what the effect of the accumulation of gas has on the accretion disk.

Our work considers the context of a boundary layer (as

opposed to an accretion column) with an accretion disk, with a sophisticated radiation treatment which deals with the optically thick and optically thin regimes. In our simulation, we will focus strictly on the effect of a reflective boundary. We will run our simulations for longer durations, $t \sim 160\,000 t_g$, where $t_g = GM/c^3$, to see what happens when a large amount of gas is accumulated in the vicinity of the neutron star.

2 NUMERICAL METHODS

We investigate accretion onto neutron stars using a sophisticated 3D General Relativistic Radiation Magnetohydrodynamics solver, KORAL used extensively to study accretion onto black hole at high and low accretion rates, and other related phenomena. Details of the numerical implementation are given in Sądowski et al. (2013, 2015). Here we describe the most relevant features.

2.1 Governing equations

The equations of GRRMHD, which can be written in their conservative form as

$$\nabla_\mu(\rho u^\mu) = 0, \quad (1)$$

$$\nabla_\mu T^\mu{}_\nu = G_\nu, \quad (2)$$

$$\nabla_\mu R^\mu{}_\nu = -G_\nu, \quad (3)$$

$$\nabla_\mu(nu^\mu) = \dot{n}, \quad (4)$$

are solved in KORAL on a static one, two, or three dimensional mesh. Our mesh is a spherical 2.5D (2D axisymmetric) grid using a static metric, $g_{\mu\nu}$ with signature $(-+++)$. Here, ρ is the gas rest-mass density in the comoving fluid frame, u^μ is the gas four-velocity, $T^\mu{}_\nu$ is the MHD stress-energy tensor given by

$$T^\mu{}_\nu = (\rho + u_{\text{int}} + p + b^2)u^\mu u_\nu + \left(p + \frac{1}{2}b^2\right)\delta^\mu_\nu - b^\mu b_\nu. \quad (5)$$

Here, u_{int} is the internal energy of the gas, and $p = (\gamma - 1)u_{\text{int}}$ is the gas pressure, calculated using the adiabatic index, $\gamma = 5/3$. The radiation stress-energy tensor is given by $R^\mu{}_\nu$ which is coupled to the gas stress-energy tensor by the radiation four-force, G_ν , making use of electron scattering and bremsstrahlung opacities as well as Comptonization Sądowski & Narayan (2015) which evolves the photon number, n , by taking into account the creation and annihilation of photons by emission and absorption, \dot{n} , while conserving n for Compton scattering exchanges of energy. The radiation stress-energy tensor is completed using the M_1 closure scheme (Sądowski et al. 2013), which assumes there is a frame in which the radiation is isotropic. The M_1 scheme allows radiation to diffuse through gas at large optical depths, and to freely stream along geodesics at very low optical depths. The magnetic field four-vector, described by Gammie et al. (2003), is given by b^μ , and it is evolved using the induction equation which, when written in the coordinate basis appears as

$$\partial_t(\sqrt{-g}B^i) = -\partial_j(\sqrt{-g}b^j u^i - b^i u^j). \quad (6)$$

Here B^i is the normal magnetic field three-vector, which is related to the magnetic field four-vector by

$$b^t = B^i u^t g_{i\mu}, \quad (7)$$

$$b^i = \frac{B^i + b^t u^i}{u^t}, \quad (8)$$

for metric g_{ij} and metric determinant, g (Komissarov 1999).

2.2 Mean-field dynamo for 2.5D runs

One particularly useful tool implemented in KORAL is a mean-field magnetic dynamo which allows for axisymmetric 2D (2.5D) accretion disk simulations to be run for long durations without depleting the magnetic field due to turbulent dissipation, which normally occurs in axisymmetric simulations of MRI (Sądowski et al. 2015). The dynamo has been tested against 3D simulations and has been found to accurately approximate the disk's spatial properties, accretion rate, surface density, and angular momentum for example. The 2D dynamo disk does however have a tendency to overestimate the magnitude and variability of the radiative flux (Sądowski & Narayan 2016). Nevertheless, the advantages of being able to run a 2D simulation as opposed to 3D make the mean-field dynamo a valuable tool, allowing for almost a 100-fold speedup in runtime, and so we chose to implement it in this work in order to run long duration simulations. We also implement an adaptation to make the dynamo more suitable to simulations where we expect a significant amount of gas to accumulate at the inner simulation boundary. We include a smooth cutoff to deactivate the dynamo in cells with a specific angular momentum lower than 80% of the Keplerian value.

3 NUMERICAL SETUP

3.1 Initial conditions

We initialize our accretion disk in a typical way by starting with an equilibrium torus near the non-rotating black hole as given in Penna et al. (2013). The torus is threaded with a weak magnetic field in loops of alternating polarity. The total pressure is distributed between gas and radiation assuming local thermal equilibrium. Once the simulation starts, the MRI quickly develops turbulence and accretion begins. We measure the rate of mass accretion in units of L_{Edd}/c^2 , where L_{Edd} is the Eddington luminosity and c is the speed of light. The initial torus is set up to give a constant accretion rate of about $200 L_{\text{Edd}}/c^2$ which would correspond to a luminosity of about $10 L_{\text{Edd}}$ for the efficiency of a Shakura-Sunyaev disk.

3.2 Boundary conditions

A common practice when simulating accretion onto stars is to ignore the effects of a hard surface and let gas flow through the inner boundary in a standard outflow boundary condition for the hydrodynamic quantities. This allows the simulation to approach a quasi-steady state and is useful for studying the interaction between the stellar magnetic field, and the accretion disk (Romanova et al. 2012; Čemeljić et al. 2013). This allows the star to behave somewhat like a black

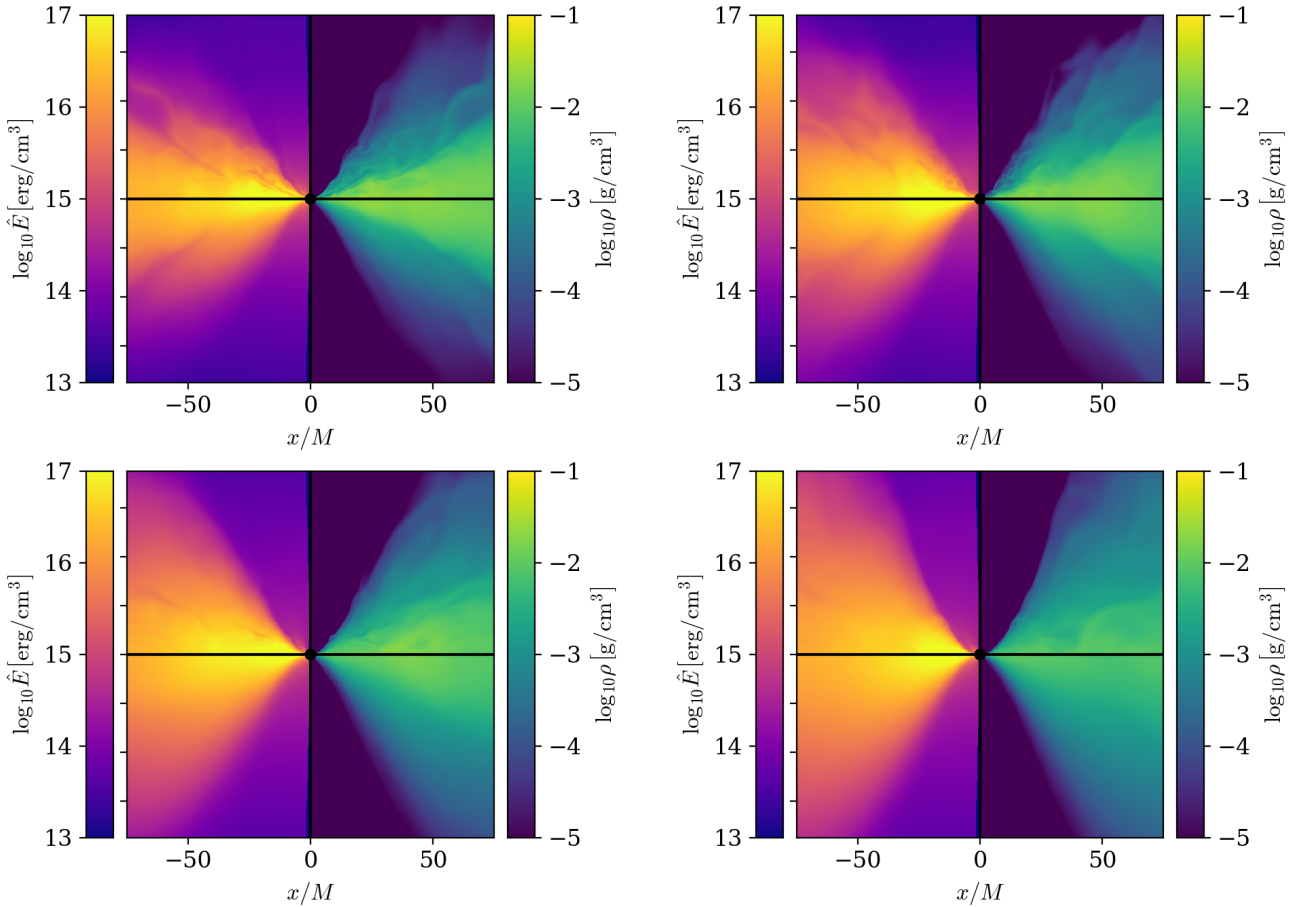


Figure 1. Here we show snapshots of the 2.5D axisymmetric simulations of super-Eddington accretion from BHRUN. The left two quadrants of each image show radiative energy density in the fluid frame, and the right panels shows the rest mass density in the fluid frame. The upper panels of each image show the instantaneous state of the simulation at time t_i , and the bottom panels are time averaged from time $t_i - t_i/3$ to $t_i + t_i/3$. From left to right and top to bottom the times correspond to, $t_i = 7500 t_g$, $15000 t_g$, $30000 t_g$, and $60000 t_g$.

hole.¹ In order to study the the difference between an inflowing boundary condition at the inner edge, and reflective boundary condition, as well as to have a natural, physical inner boundary as a baseline comparison, we run one simulation with a black hole as the inner boundary condition. This is achieved by choosing a horizon penetrating coordinate system (Kerr-Schild) and placing the inner boundary of the simulation sufficiently behind the event horizon. This simulation we call BHRUN.

In order to study the effects of the release of kinetic energy, which is expected to significantly impact the behavior of the accretion disk and outflows, we implement a reflective boundary for the main simulation of our study. The reflective boundary at $r = r_{\text{in}}$ is set up so that the reconstructed radial velocity of the gas at the inner boundary is opposite about zero ($u_l^r = -u_r^r$ where u_l^r, u_r^r are the left and right reconstructed radial velocities at the cell interface of the inner boundary), so that no gas is able to leave the domain. We also set the tangential velocities u^θ, u^ϕ in the ghost cells to zero. Note that this does not enforce the reconstructed

tangential velocities to be exactly zero at the inner boundary, it does however effectively remove angular momentum and allows the gas to approach a non-rotating state at the inner boundary, and so we expect the formation of a boundary layer. Radiative quantities are treated in the same way. We expect these boundary conditions to more accurately reflect the behavior of an accretion disk and a boundary layer around a neutron star than an inflow boundary condition, and so this simulation we call NSRUN.

3.3 Grid

Both simulations are run in Kerr-Schild coordinates (although this is not strictly necessary for NSRUN) with a non-rotating, central mass of $M = 1.4M_\odot$ (Schwarzschild spacetime). We run two simulations on identical 2D, axisymmetric spherical grids with logarithmic spacing in radius, and increased resolution near the equatorial plane. The resolution for NSRUN is $N_r \times N_\theta \times N_\phi = 352 \times 240 \times 1$. The radial coordinate spans from $r_{\text{in}} = 5r_g$ to $r_{\text{out}} = 5000r_g$ where $r_g = GM/c^2$. The resolution was higher for BHRUN ($N_r \times N_\theta \times N_\phi = 384 \times 240 \times 1$) because we have to extend the inner boundary to below the event horizon at $r = 2r_g$. The

¹ This is not entirely true, there are a variety of inner boundary conditions on the magnetic field quantities that have various effects on the absorption of the hydrodynamic quantities.

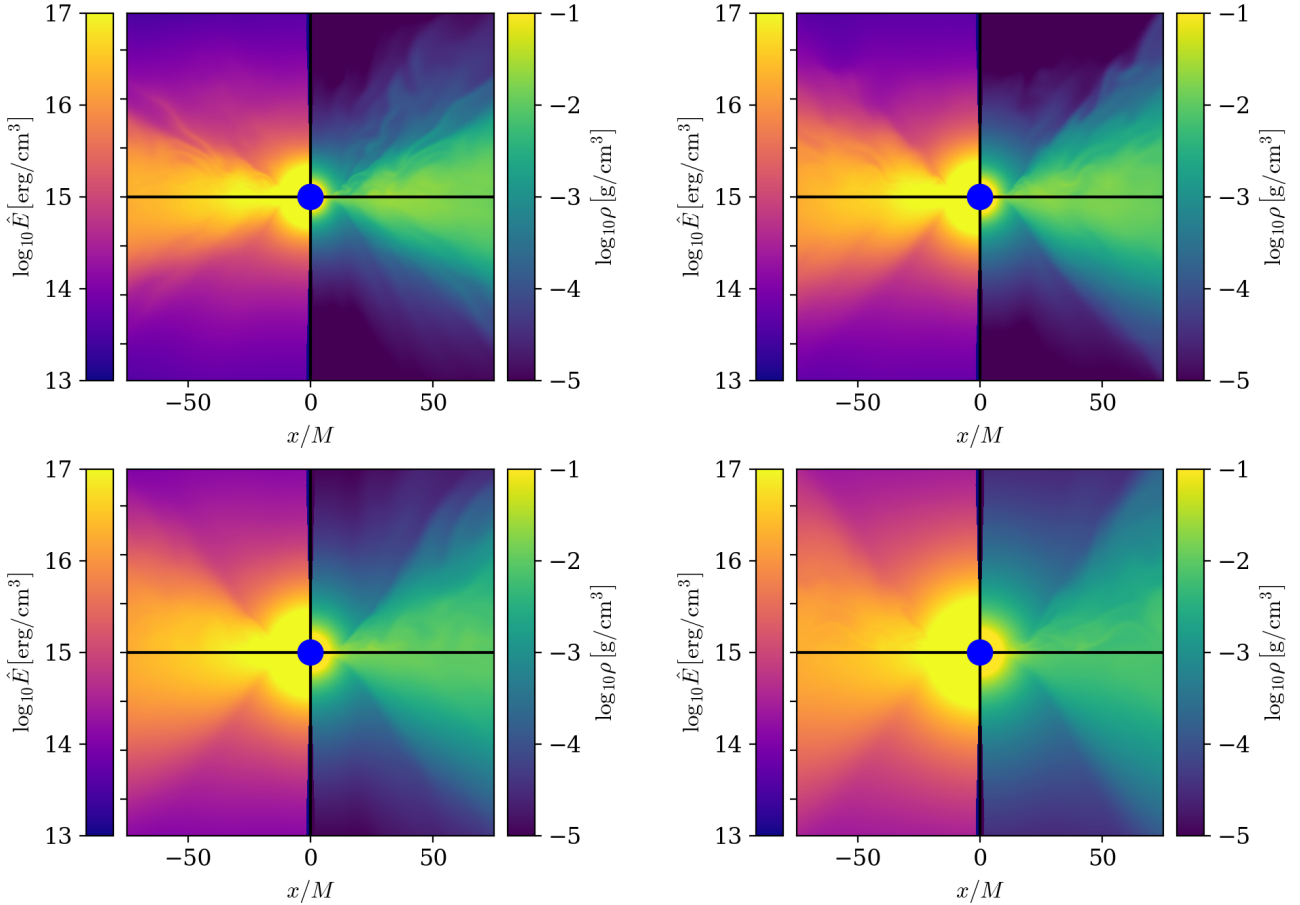


Figure 2. Here, using the same scheme as in Fig. 1, we show four snapshots of NSRUN, the simulation with the reflective boundary condition.

larger number of radial grid cells allows the two simulations to have comparable resolution at the same radii.

4 RESULTS

We have run two axisymmetric GRRMHD simulations, one with a reflective, non-rotating inner boundary at radius $r = 5r_g$ NSRUN, and one with a black hole inner boundary, BHRUN. Snapshots and time averages of both simulations are shown in Figs. 1 & 2. Each figure contains four images, each corresponding to a different time, $t_i \in \{7500 t_g, 15000 t_g, 30000 t_g, 60000 t_g\}$. Snapshots at these times are shown in the upper two quadrants of each image. We are also showing the time averaged structure of the simulations in the lower two quadrants of each image, all of which are averaged from $t = t_i - t_i/3$ to $t = t_i + t_i/3$. The right two quadrants of each image show rest mass density, and the left two quadrants show radiation energy density in the fluid frame.

The BHRUN simulation forms a typical, geometrically thick, super-Eddington accretion disk similar to what is seen in previous simulations of this type, see Yang et al. (2014); Jiang et al. (2014); Sądowski et al. (2015); Sądowski & Narayan (2016); Ogawa et al. (2017) for examples. As the disk reaches inflow equilibrium one can see the formation of

a funnel region along the polar direction. The funnel region is nearly devoid of gas but is filled with radiation and so one can expect the disk to appear very bright when viewed along the funnel.

The reflective inner boundary shows a much different scenario. Gas cannot pass through the inner boundary, so it accumulates a dense layer around the inner edge of the simulation. At late times, the density at the inner edge reaches nearly 10 g/cm^3 . The density at the inner edge increases gradually as more and more gas is compressed into the atmosphere. We can also see large amounts of radiation being accumulated at the inner boundary due to a combination of dissipation and advection. In general, hot flows of this type are optically thick to scattering, but optically thin to absorption. However, it is unclear a priori if the radiation can escape to infinity in any reasonable amount of time because gas is blown off the outer edges of the accumulating layer which forms a dense outflow. Photons produced near the disk must random walk through this thick outflow, some of them may even be scattered back through the disk. We are particularly interested in whether or not pulsations may be visible. With such a thick scattering dominated atmosphere, it is likely that pulsations would lose their coherence. We measure the scattering optical depth in the next subsection.

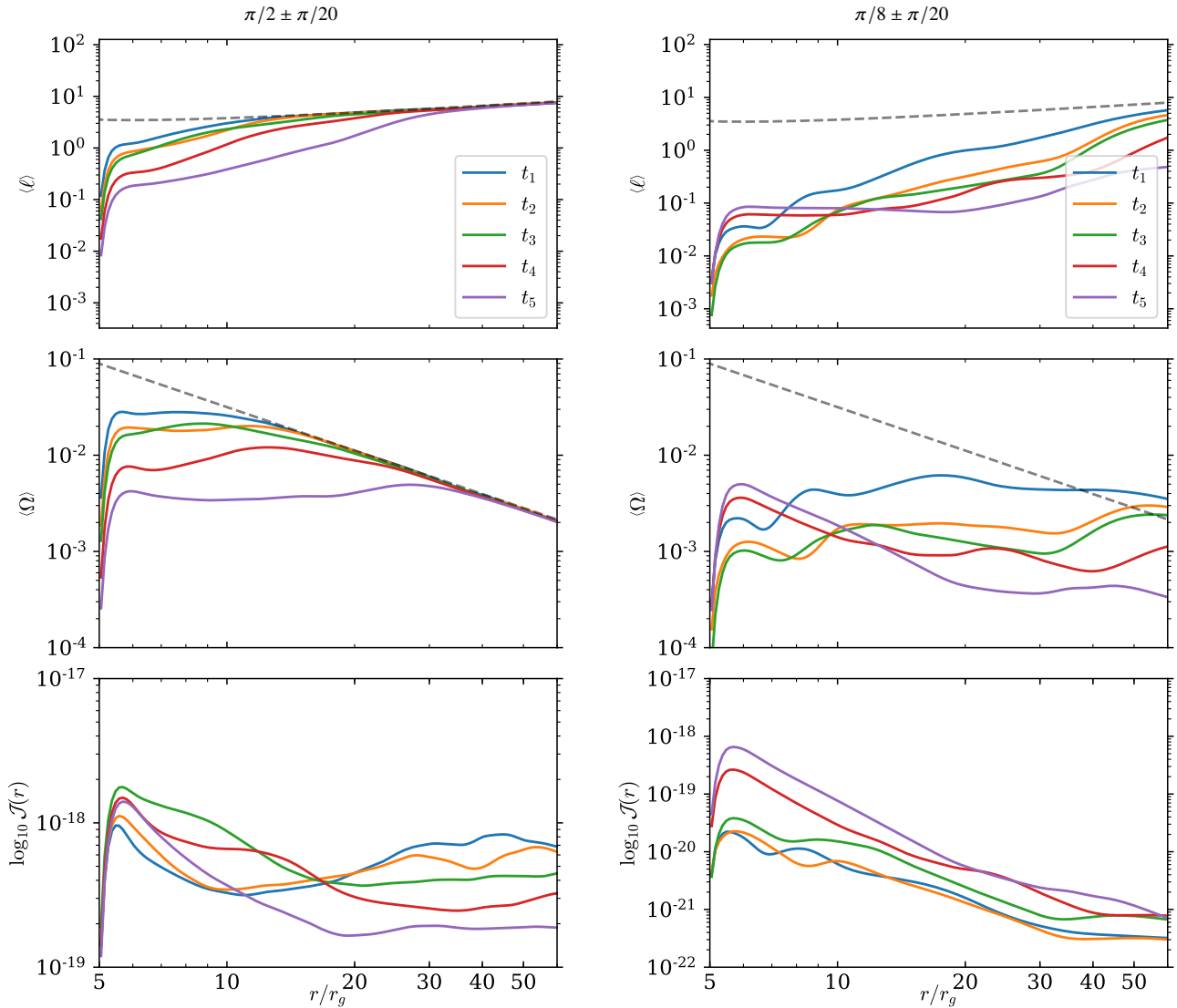


Figure 3. We plot angular momentum related quantities in the disk mid-plane ($\theta = \pi/2$, left) and in the polar region of the simulation ($\theta = \pi/8$, right). The plots were averaged/integrated over a range of angles corresponding to $\pi/10$ radians. Top: Here we show a time series of the specific angular momentum of the gas, $\ell = u_\phi$ for NSRUN. The plotted quantities correspond to a ρ -weighted θ -average of the time averaged simulation data. The durations for the averaging are the same as for Fig. 1 & 2, $t_1 = 7500 t_g$, $t_2 = 15000 t_g$, $t_3 = 30000 t_g$, $t_4 = 60000 t_g$ with an additional time interval centered at, $t_5 = 120000 t_g$. The Keplerian angular momentum is shown by the dashed grey line. Middle: Here is the same plot as above except for angular velocity, $\Omega = u^\phi/u^t$. Bottom: Here, we are plotting the total angular momentum density integrated along the θ direction.

4.1 Transition layer and accretion disk structure

The inner boundary of the neutron star simulation causes the angular velocity of the gas to approach zero. This is seen in Fig. 3. The top panels of Fig. 3 show the density-weighted, θ -averaged profiles of the specific angular momentum of time averaged time intervals used in Figs 1 & 2 for NSRUN. Because NSRUN is computationally cheaper compared to BHRUN and because the behavior at late times is interesting we run NSRUN for an additional 80 000 t_g so that we can show an additional time interval in Fig. 3, $t_5 \sim 120000 t_g$. The left three panels show the midplane quantities, averaged or integrated over a range of θ from $\pi/2 - \pi/20$ to $\pi/2 + \pi/20$. The right three panels are integrated in the polar region, over θ from $\pi/8 - \pi/20$ to $\pi/8 + \pi/20$. As the simulation evolves, we

can see the formation of a transitional region which expands outwards as more gas is accumulated. The rate of expansion measured by calculating the radius at which ℓ reaches 90 percent of its Keplerian value follows a $t^{0.85}$ power law. For accretion onto neutron stars at lower accretion rates, this transitional layer usually lies in a small belt around the star where the flow properties transition to match the stellar surface. This is the classical picture of a boundary layer. We can see from Fig. 2 that we have a much more extended, atmospheric layer, although the flow velocity does transition to match the surface of the neutron star, so we will refer to this region as the transition layer.

The process by which angular momentum is transferred from the accretion disk to a neutron star is complicated. Various viscous and magnetic processes are involved.

We try to reproduce the effect of driving the tangential velocity to zero at the inner edge of the simulation with our inner boundary condition. The normal magnetoturbulent processes that transport angular momentum through the disk do not operate on the numerical level of the cell interface. Instead angular momentum is transported between cells according to the flux computed by the HLL Riemann solver. The angular momentum flux is made up of a hydrodynamic and a magnetic component, $T_{r\phi} = T_{r\phi}^{(\text{HD})} + T_{r\phi}^{(\text{mag})}$ where $T_{r\phi}^{(\text{HD})} = (\rho + u_{\text{int}} + p)u_r u_\phi$ and $T_{r\phi}^{(\text{mag})} = b^2 u_r u_\phi - b_r b_\phi$. By far the largest contribution at the inner edge is the $\rho u_r u_\phi$ term. The inner boundary condition leads to a flux that is approximately, $T_{r\phi} \approx \rho u_r u_\phi / 2$. Reflecting the angular velocity, for example, would lead to $T_{r\phi} \approx \rho u_r u_\phi$. We can see that the source of the torque at the inner edge is numerical in nature. A more detailed study of the effect of different boundary conditions on the transport of angular momentum through the transition layer is left to further studies. For now, we are satisfied the angular momentum transitions towards zero at the inner boundary through the midplane and along the disk axis.

The middle two frames of Fig. 3 show angular velocity averaged in the same way as the top panels of Fig. 3. We can see the expansion of the transition layer evolving into a quasi-flat region in angular velocity in the midplane indicating that some large scale coupling is causing the inner disk to rotate like a rigid body. The innermost region is driven towards zero angular velocity as is expected by the boundary condition.

The polar region shows different behavior. The angular momentum in the polar regions increases with radius at early times, and evolves to be quasi flat at late times in the inner region. Meanwhile, the angular velocity starts quasi flat, and evolves to decrease with radius at late times, so the transition layer does not display rigid body behavior near the poles.

As is seen in Fig. 2, the transition layer reaches very high densities, and so, even though it has very low angular velocity, it is still able to contain a significant amount of angular momentum, as shown in the bottom panels of Fig. 3. Here we are plotting the angular momentum integrated at a particular radius, r , $\mathcal{J}(r) = 2\pi \int \rho u_\phi \sqrt{-g} d\theta$. The total angular momentum in the transition layer increases with time, especially near the inner edge. Angular momentum is transported through the transition layer where it accumulates at the inner edge. It is likely that a stronger numerical torque at the inner edge would allow more angular momentum to flow through the inner boundary, thus smoothing \mathcal{J} near the neutron star surface. Dynamically, what is important are ℓ and Ω , both of which are largely below their corresponding Keplerian values, and so we do not expect a stronger torque at the inner boundary to have a significant effect on the evolution of the simulation.

The transition layer does not display much structure in the spatial distribution of gas density and radiation energy density, except for a strong radial gradient, even when the color scales are suitably adjusted. The flow structure is much more informative.

In Fig. 4, we show the time-averaged spatial distribution of the poloidal velocities in the two upper panels for the time interval, t_4 from 40,000 t_g to 80,000 t_g . All of the remain-

ing figures are constructed with time averaged data over the same period. The poloidal velocity and accretion rate are defined as follows, $u^{\text{pol}} = \sqrt{u^r u_r + u^\theta u_\theta}$, $\dot{M}_{\text{pol}} = 2\pi r^2 \sin \theta \rho u^{\text{pol}}$. For BHRUN, the flow is primarily directed inward in the disk and at the inner boundary. This is a boundary condition imposed by the space-time. In the polar region, one can see the transition from inflow to outflow at about radius of $r = 10r_g$. This is the stagnation radius, above which is a radiation driven outflow. Velocities in the polar region are relativistic, while velocities in the disk are around a few hundredths of the speed of light except in the very inner regions.

Again, NSRUN shows a much different inner structure. Gas flows through the transition layer in the equatorial plane where it meets the reflective boundary and is directed tangentially along the surface of the inner boundary until the polar regions where it is again redirected. The whole process forms two large eddies which seem to recycle the gas into the inner edge of the accretion flow, which could be responsible for the large scale coupling seen in Fig. 3. The eddies seem to be connected to a conical outflow. We can see two streams of gas being launched from the two regions where the eddy circles back to the disk. It is important to note that this is the time average structure, the non-averaged flow being much more turbulent. The eddies are indicative of convective cells. Indeed, a calculation of the Schwarzschild stability parameter shows that the transition layer should be unstable to convection. Whether convection is driving the eddy motion is more difficult to say due to the extra source of momentum from the accretion flow.

The poloidal accretion rate is shown in the middle two panels of Fig. 4 over a large range in r and z . The accretion rate in the transition layer is nearly an order of magnitude higher than in the disk, indicating that the gas is recycled many times in the inner flow. For BHRUN, we see the typical picture of a nearly empty funnel region, indicating that most of the outflowing gas is ejected in a wind at larger radii.

We expect a much different picture in the presence of strong magnetic field. For $\mu \gtrsim 10^{30}$ G cm³, we expect the accretion flow to be directed along magnetic field lines and deposited at the poles for a dipolar magnetic field as was seen in Takahashi & Ohsuga (2017). The magnetic field would also arrest any outflows from the inner most regions, so it is likely that an optically thin funnel would also be able to form in this case, leading to much larger observed luminosities.

We show the poloidal accretion rate over an even larger range of r and z in the lower two panels of Fig. 4. We can no longer see the structure of the conical outflows in NSRUN which was decollimated at larger radii. We also show a contour of the relativistic Bernoulli number in green, $Be = 0$, which we define and discuss in more detail in Section 4.2. We can clearly see that more material is launched in NSRUN than in BHRUN.

The region behind the initial torus in our simulation is unphysical. In a real physical system this region would be occupied by the gas flowing from the companion star. We exclude this region in a somewhat arbitrary way. We pick the last streamline which originates from the surface defined by $Be = 0$ (shown in white) which does not turn back towards the disk midplane at larger radii. The gas inside this region is expected to flow back towards the disk or to the

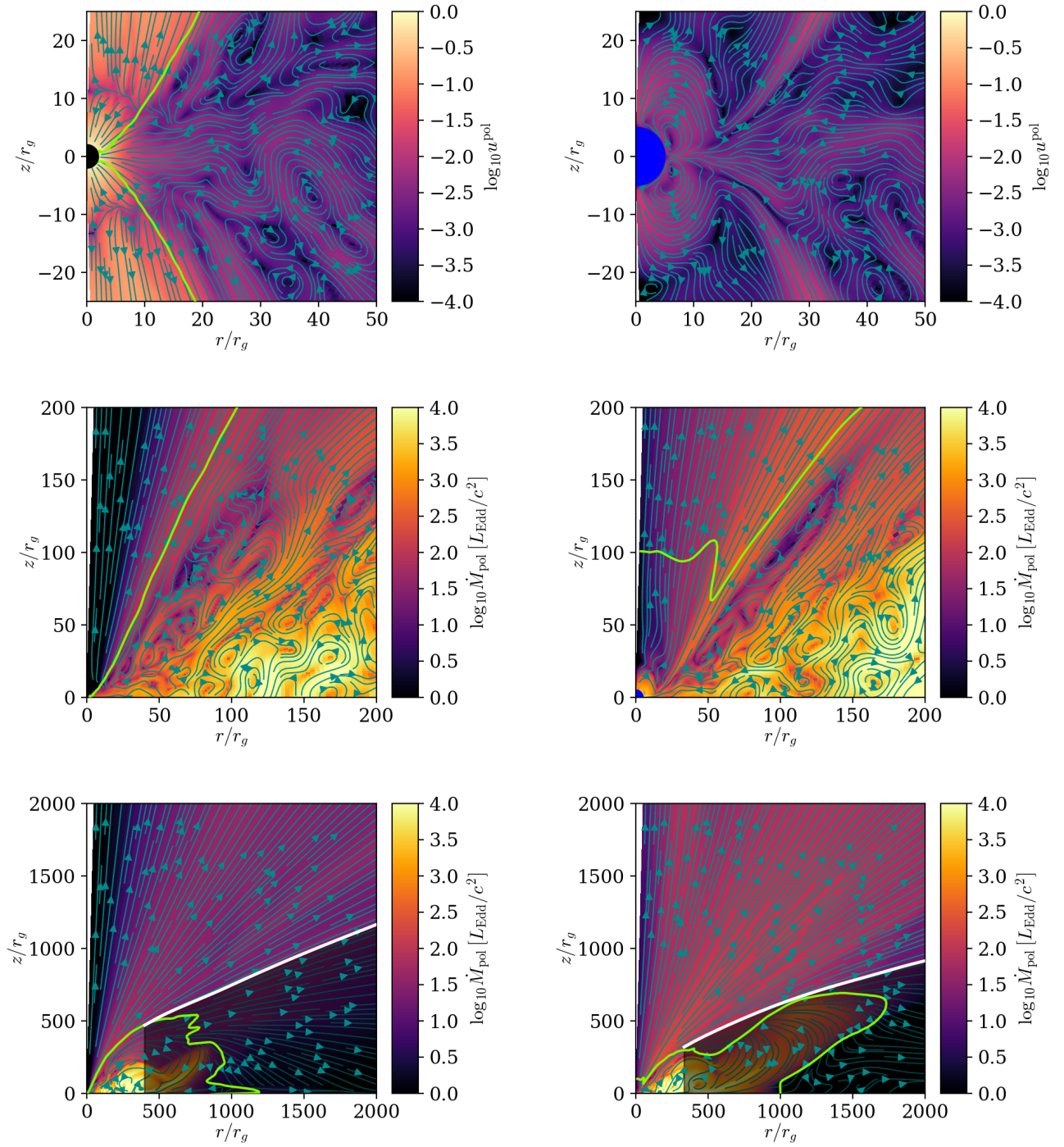


Figure 4. Here we show the time averaged poloidal velocity flow structure of the black hole-like simulation (upper-left) and reflective simulation (upper-right). The magnitude of the poloidal velocity ($u^{\text{pol}} = \sqrt{u^r u_r + u^\theta u_\theta}$) is given by the color map. The streamlines follow the poloidal velocity vectors for all plots in the figure. The middle two images show the mass accretion rate in the poloidal plane ($\dot{M}_{\text{pol}} = 2\pi r^2 \sin\theta \rho u^{\text{pol}}$) for BHRUN simulation (middle-left) and NSRUN (middle-right). The two bottom images are the same as for the middle images, except for a larger range of r and z . We show a contour of $Be = 0$ in green and in white we show the last streamline which originates from the $Be = 0$ surface. The shaded region below, we exclude from our analysis.

companion star, and so we exclude this region from all of our calculation.

In Fig. 5 we show the time averaged (again, over t_4) spatial structure of both disks. The colormap of density has been expanded to cover a wider range of densities with the trade off being a lack of detail. We show two zoom levels. Red, white, and green contours of the scattering optical depth are also shown. From green to white to red, the contours correspond to $\tau_{\text{sca}} = 0.01, 0.1, 1, 10, 100$. Here, τ_{sca} is calculated in a simple way,

$$\tau_{\text{sca}}(r) = \int_r^{r_{\text{out}}} \rho \kappa_{\text{es}} \sqrt{g_{rr}} dr, \quad (9)$$

where $\kappa_{\text{es}} = 0.34 \text{ g cm}^{-2}$. For reference, the root-mean-squared polar scale height of the disk defined by $h = \sqrt{\int (\theta - \pi/2)^2 \rho d\theta / \int \rho d\theta}$. For BHRUN (left), super-Eddington accretion leads to a thick disk with strong outflows and an optically thin funnel region reaching all the way down to the inner boundary. Again, we see a different picture for NSRUN (right). First, as is also seen in Fig. 2 a large amount of gas is deposited in a transition layer around the inner edge. In addition, a large amount of gas is ejected and the entire domain is filled with a thick outflow. Measuring the optical depth shows that this outflow is extremely optically thick. The last contour of the scattering optical depth visible in the figure is given by the red line which corresponds to τ_{sca} of 100. A zoom of the entire simulation domain is shown in the bottom two panels. We can see the photosphere for NSRUN lies on average at a couple thousand r_g , which is indicated by the white line.

In Fig. 6 we show the radial profiles of both simulations. BHRUN and NSRUN are shown in blue and orange, respectively, for the time interval t_4 . The green lines shows the later evolution of NSRUN over time interval t_5 . The first quantity shown is the surface density,

$$\Sigma = \int_{\pi/2-h}^{\pi/2+h} \rho r \sin \theta d\theta \quad (10)$$

integrated within one scale height. The three remaining plots correspond to density weighted, θ averages, which for a given quantity f , appears as

$$\langle f \rangle = \frac{\int_{\pi/2-h}^{\pi/2+h} \rho f \sqrt{-g} d\theta}{\int_{\pi/2-h}^{\pi/2+h} \rho \sqrt{-g} d\theta}. \quad (11)$$

The scale height captures a majority of the mass in BHRUN and can be a reasonable approximation for the boundary of the accretion disk. It becomes a less useful tool however in the inner edge of NSRUN, where the distribution of density becomes roughly spherical, and the distinction between disk and transition layer requires more information. Nevertheless, this only affects the weighting of the quantities, which, if they are also roughly spherical, should still give a good measure of the radial profile. We can see that the transition layer surface density follows a power law before settling into the accretion disk which matches that of the black hole at about radius $r = 30 r_g$. The second panel shows $\langle u^r / c \rangle$, the density weighted radial component of the four velocity. The inflow velocity for NSRUN remains nonrelativistic. The local maximum at the inner edge is related to the circularization pattern seen in Fig. 4. The third panel shows density

weighted temperature, $\langle T \rangle$. The temperature inside of the atmosphere approaches $10^{8.5} \text{ K}$, and also follows a power law at the inner edge. We also measured the growth rate of the temperature on the surface of the neutron star and found that it grows with a $T(t) \propto t^{1/4}$ dependence. The last panel shows the density weighted ratio of angular velocity to the Keplerian angular velocity, $\langle \Omega / \Omega_k \rangle$. We can also see the angular velocity transition towards zero as observed in Fig. 3. The accretion disk is mildly sub-Keplerian.

4.2 Outflow and luminosities

Accurate measurements of the outflow from black hole and neutron star accretion disks are important for estimating feedback on the surrounding media of these systems. We measure the radiative and kinetic luminosities of our accretion flows as well as the mass outflow rates. We purposely chose a very large simulation domain so that we can measure these quantities out to larger radii, however, these measurements are meaningless without indication that the simulation has reached some sort of equilibrium. Typically, this is measured by computing the viscous time of time averaged data over a particular interval, and seeing at which radius the viscous time is equal the length of that time interval (Narayan et al. 2012). This roughly corresponds to about $r = 80 r_g$ for our simulations averaged over time interval t_4 , evidence of which can be seen in Fig. 6 where the averaged radial velocity changes sign at about $100 r_g$, an indication that inflow equilibrium has not been reached passed this radius. This means that we can trust the results of our simulation inside radius $r = 80 r_g$.

Outside $80 r_g$ however, we can still trust the results of the outflow, as long as it is causally connected to the converged region inside radius $r = 80 r_g$. Because the velocity of the outflow is much higher than that of the inflow, this corresponds to much larger radii where we can reliably measure the outflow. To quantify this, we measure the density weighted average velocity, $\langle u^r \rangle$ as a function of radius. We take the average over the θ coordinate only for cells with $Be > 0$ to reasonably track outflowing gas. Here, Be is the relativistic Bernoulli number,

$$Be = -\frac{T^t_t + R^t_t + \rho u^t}{\rho u^t}. \quad (12)$$

In steady state, Be is conserved along streamlines and gas with positive Be is energetic enough to escape to infinity, and so it is a reasonable parameter to define the outflow. Separating the outflow from the disk flow is not precise, so one should not put too much influence on the Bernoulli parameter. For example, we can see from Fig. 4 that the outflow from near the neutron star transition layer appears to change Bernoulli parameter. We have investigated this further and found that when looking at the non-time-averaged data in this particular region, the flow does not appear to be steady, and the $Be = 0$ surface is highly variable. For steady flows (such as the outflow at larger radii, the Bernoulli parameter should still be appropriate for calculating r_{cc}

We use time averaged data for the time interval, t_4 , from $40,000 t_g$ to $80,000 t_g$, and multiply the time and θ -averaged velocity by the duration of the time interval, $\Delta t = 40,000 t_g$ to find the causally connected radius, r_{cc} , for an outflow of that velocity. This assumes a constant velocity

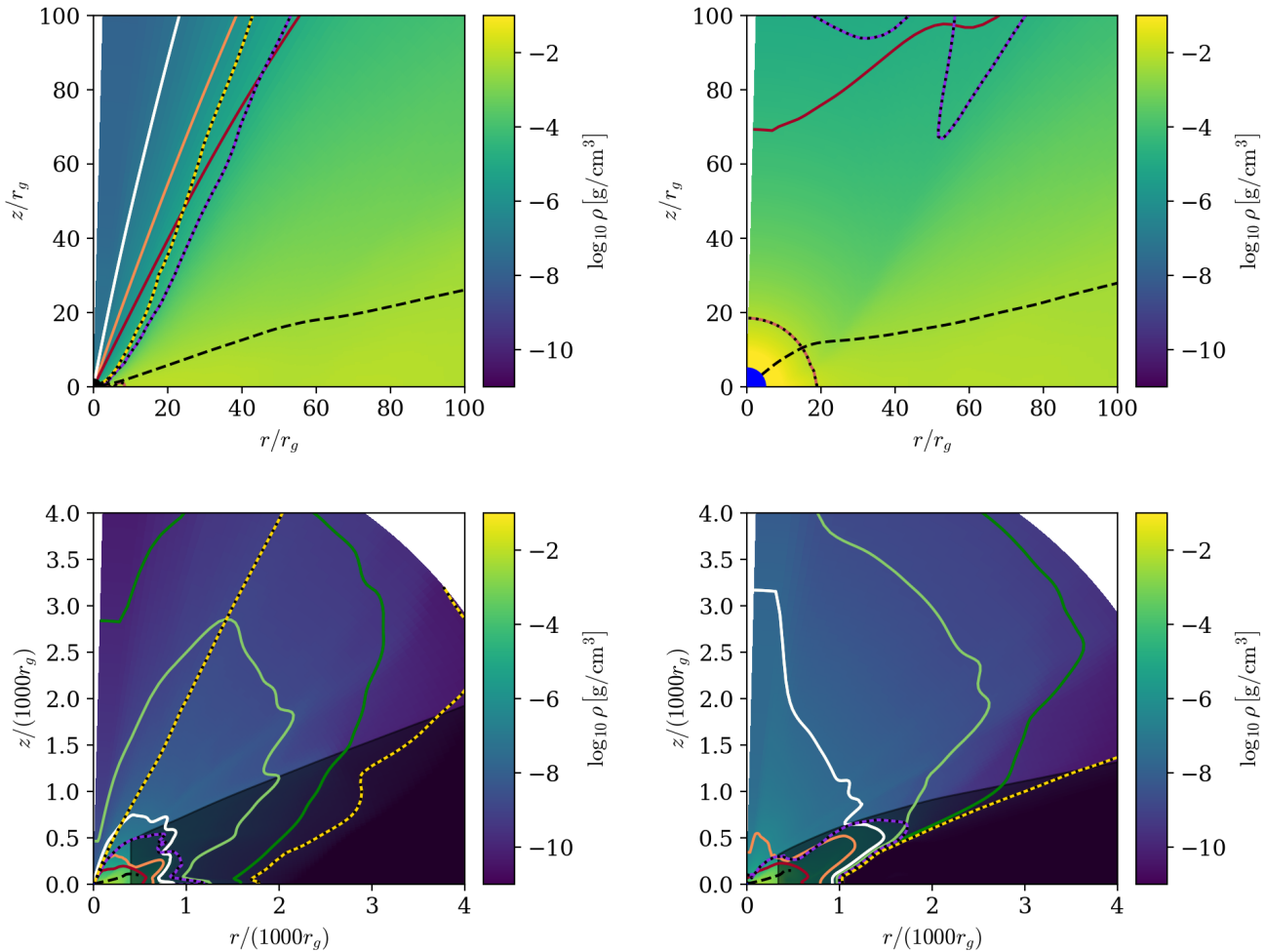


Figure 5. Here we show the time averaged structure of the BHRUN (top-left) and the NSRUN (top-right). Expanded views of the simulations are shown in the bottom panels. The colormap shows density. The colored contours correspond to optical depth to scattering. From green to red the values correspond to $\tau_{\text{sca}} = 0.01, 0.1, 1, 10, 100$. The white line shows $\tau_{\text{sca}} = 1$. The striped red, purple, and yellow lines show contours of $Be = -0.05, 0, 0.05$ respectively. The dashed black line shows the rms scale height, h . We have also darkened the region contained by the last streamline to originate from the $Be = 0$ surface.

along the outflowing trajectory, however, since velocity tends to decrease with radius, the causally connected radius we find is a lower limit. Then, as long as the causally connected radius is larger than the radius where we are measuring the velocity, we can believe the results of the outflow. A plot of r_{cc} is shown in Fig. 7. We can see that the outflow of BHRUN is reliable throughout the entire outflow region excluding the region behind the initial torus shown in Fig. 4. For NSRUN, it is reliable to about $r \approx 4000r_g$. It is important to note that this analysis does not take into account changes in the nature of the outflow with time, but only that the outflow is causally connected to the central region of the simulation.

An additional issue which must be addressed is contamination of the results by the initial condition. Our initial condition is an equilibrium torus where the total pressure has been distributed between gas and radiation. The torus is constructed assuming radiation pressure domination, which implies an adiabatic index, $\gamma = 4/3$. However, the effective adiabatic index depends on the particular mix of gas and radiation at a particular position, and so does not everywhere

equal $4/3$, especially in cooler parts of the torus. For this reason, the torus is not in perfect hydrostatic equilibrium. There is also a certain amount of gas that is blown off of the outer edges of the torus due to radiation pressure. However, the whole torus was constructed with $Be < 0$, and so due to the lack of dissipation or viscosity in the regions in the outer parts of the torus where the MRI has yet to develop, there is a reasonable expectation that Be remains less than zero. Therefore, by measuring the outflowing quantities over regions with $Be > 0$, we are reasonably screening the contamination by the initial condition. Additionally, this region overlaps significantly with the area excluded by the last streamline from the $Be = 0$ surface. We can see which region this corresponds to by examining the purple dashed line in Fig. 5. This region is relatively small compared to the computational domain of the simulation. A more robust diagnostic would be for example, evolving a tracer along with the simulation to track the evolution of gas. Then it would be possible to check whether the gas originated from the inner, converged regions of the simulations or not.

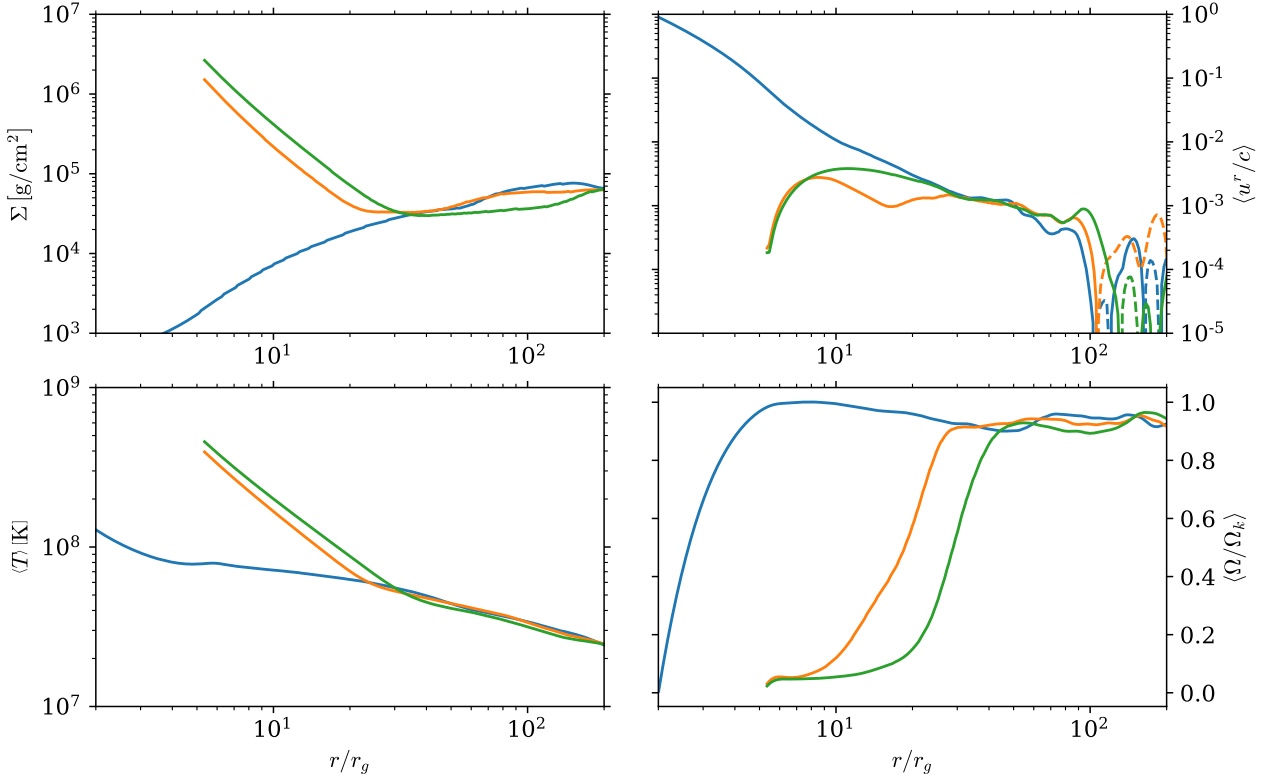


Figure 6. Here we show radial profiles of surface density, Σ , density-weighted, θ -averaged inflow velocity, the density-weighted, θ -averaged temperature, and the density-weighted, θ -averaged ratio of angular momentum to the Keplerian angular momentum. The data is time averaged over the range, t_4 from $40\,000 t_g$ to $80\,000 t_g$ and θ -averaged over one scaleheight, h . Plots are shown for the both BHRUN (blue) and NSRUN (orange). We also plot in green the same quantities from NSRUN time averaged over the interval t_5 from $80\,000 t_g$ to $160\,000 t_g$.

In Fig. 8, we show the angular distribution of radiative flux, $F^r = R^r_t$, as a function of θ . The units of the flux are given in the inferred isotropic luminosity by multiplying by $4\pi r^2$. We plot the flux at four different radii, $50r_g$, $500r_g$, $2000r_g$, $4000r_g$. We have emphasized the regions where the gas is optically thin, as the radiation in the optically thick regions is not expected to reach the observer. The optically thick regions should not be completely ignored however, it is still possible for the outflowing matter to add or subtract from the radiation field, and so it is difficult to say what the distribution of radiation will look like at infinity. The BHRUN behaves as expected. The optically thin funnel region produces locally super-Eddington fluxes. We can see that the radiation is highly collimated, even at large radii. The intensity of radiation increases with radius at lower radii, and decreases at larger radii, as the disk and outflowing gas emit and absorb radiation. NSRUN is more complicated however. Due to the thick outflows the photosphere is pushed nearly to the edge of the simulation domain. Only at very large radii can we measure a flux of locally about Eddington. Larger accretion rates may be required to reach higher luminosities, although it is hard to say whether or not the increase in outflowing gas will cancel any increase in luminosity. Indeed, in the case of black holes, it is well known that at super-Eddington accretion rates, an increase in the accretion rates corresponds to a decrease in the radiative efficiency so that the luminosity scales loga-

rithmically, $L \propto \log(1 + \dot{M}/\dot{M}_{\text{Edd}})$ (Shakura & Sunyaev 1973). It may even be interesting to try smaller accretion rates in case the outflow scales differently than the luminosity in the presence of a reflective boundary condition.

Besides observational properties, the implications of black hole feedback play an important role in the astrophysics of star formation, star clusters, and galaxies. In Fig. 9, we show the luminosity of kinetic energy, defined as,

$$L_{\text{KE}} = 2 \times 2\pi \int_0^{\theta_{\text{out}}} -(u_t + \sqrt{-g_{tt}})\rho u^r \sqrt{-g} d\theta, \quad (13)$$

where θ_{out} is the angle at which $Be = 0$. By integrating over positive Be , we are choosing only the gas which is energetic enough to reach infinity. The extra factor of two reflects the fact that we include the contribution from both sides of the equatorial plane. In the non relativistic limit, the integrand approaches $1/2\rho v^2 v^r$, where v^i is the three-velocity, v^2 is the square of the three-velocity, and v^r is the radial component of the three-velocity. NSRUN shows a large amount of material ejected into the surroundings of the neutron star environment. A large amount of it remains bound and so only at around $r = 100r_g$ is $\theta_{\text{out}} > 0$. NSRUN everywhere has a less energetic outflow than BHRUN, leveling off at $L_{\text{KE}} \approx 0.4L_{\text{Edd}}$. For BHRUN the gas is energetic enough to escape to infinity in the funnel region even at radii below the stagnation radius, however the velocity vector is directed inward and so

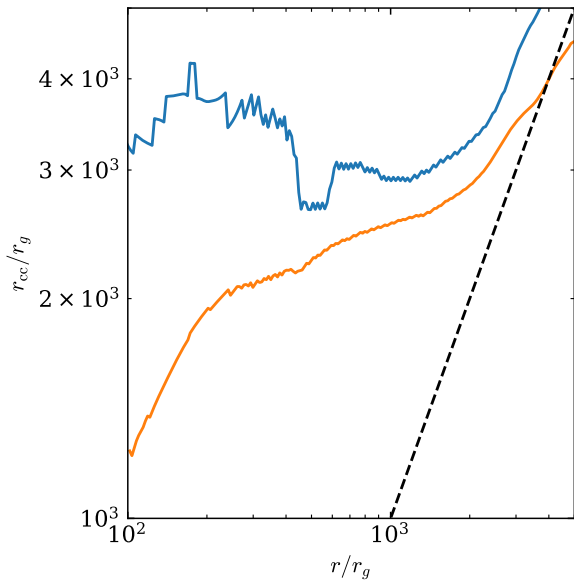


Figure 7. Here we demonstrate the convergence of the outflow by plotting the radius causally connected to the inner region of the disk, r_{cc} , as a function of the radius at which measure the velocity, r . For $r_{cc} > r$ we can reliably measure the outflow of the simulation. For reference, $r = r_{cc}$ is shown by the black dashed line. As with Fig. 6, blue corresponds to BHRUN and orange to NSRUN. If $r_{cc} > r$, then the gas had enough time to reach radius r .

the flux of kinetic energy is into the inner boundary, thus the transition to negative values in the kinetic luminosity.

The total radiative output of the simulation is difficult to measure directly, especially for optically thick flows. Radiation and gas can still exchange energy even after the gas has left the simulation domain. We chose to run our simulations with a very large outer radius, so that the photosphere is still contained in the simulation. This allows us to measure the amount of radiative energy outflowing from optically thin and outflowing regions. Radiation flowing through optically thin regions is expected to escape to infinity, and so is an effective lower limit on the total radiative output. We define the optically thin region by the angle at a particular radius where the radial scattering optical depth is equal to one. For each radius, we integrate the radial radiative flux over the optically thin region,

$$L_{\text{thin}} = 2 \times 2\pi \int_0^{\theta_{\text{thin}}} -R^r_t \sqrt{-g} d\theta. \quad (14)$$

A reasonable upper limit of the radiative luminosity, is the integral of F^r over the region of $Be > 0$, L_{out} , as in the calculation of L_{KE} . This gas is energetic enough to reach infinity, and so it is possible for the outflowing gas to eventually release its trapped photons. Note that it is possible for this gas to produce additional photons, but this is not thought to contribute significantly to the radiative luminosity, so L_{out} is not a strict upper limit. The outflowing luminosity is then given as,

$$L_{\text{out}} = 2 \times 2\pi \int_0^{\theta_{\text{out}}} -R^r_t \sqrt{-g} d\theta \quad (15)$$

The outflowing and optically thin radiative luminosities are shown in Fig. 10. In general BHRUN shows about two to three times as high luminosity as NSRUN. As shown in Figs. 1 & 2, NSRUN produces a much larger amount of radiation energy. However, the vast majority is trapped in the optically thick outflow and transition layer. We also observe a general decrease in luminosity at radii larger than about $300r_g$. This is because of radiation flowing into the excluded regions behind the initial torus. The optical depth of this region is low and so radiation can escape from the outflow into this region. It is hard to say how the radiation would behave in this region in reality, it would depend on the extent and thickness of the accretion disk. We do not seem much change in the radiative luminosity over the t_5 time interval.

Super-Eddington accretion flows are known to have strong radiation driven outflows (Ohsuga et al. 2005; Hashizume et al. 2015; Fiacconi et al. 2017). We can measure this by examining the accretion rate in a few different ways. First in the top panel of Fig. 11, we measure the total (net) mass accretion rate as a function of radius,

$$\dot{M}_{\text{tot}} = 2\pi \int_0^\pi -\rho u^r \sqrt{-g} d\theta. \quad (16)$$

BHRUN, which is shown in blue, gives a flat accretion rate out to about $r \lesssim 50r_g$, which roughly corresponds to the region where the simulation has achieved steady state. NSRUN, shown in orange, is also nearly flat for a small region between $20r_g$ and $50r_g$. At low radii the simulation is accumulating mass, which corresponds to a non-flat slope of \dot{M}_{tot} . In general, \dot{M}_{tot} is lower for NSRUN than for BHRUN. This is not due to a lower accretion rate in the disk, but due to the fact that the gas that is normally lost through the inner boundary of BHRUN either accumulates in the transition layer where it is recycled into the inner accretion flow, or is ejected into the outflow, the latter of which contributes to a lower value of \dot{M}_{tot} . We also show \dot{M}_{tot} for NSRUN averaged over the time interval t_5 . We can see that the flat region indicating an accretion disk in steady state is no longer present. This is due to two effects. The first is the transition layer increasing in radius. The second is due to the fact that the outflows are increasing at higher radii and so the total accretion rate over the whole sphere decreases.

The second panel of Fig. 11 shows the inflowing accretion rate as measured in two different ways. The first is a more naive measurement of the inflow accretion rate,

$$\dot{M}_{\text{in},u^r} = 2\pi \int_{u^r < 0} -\rho u^r \sqrt{-g} d\theta,$$

where we simply sum over individually inflowing cells. These are the solid curves in the second panel, and in general, BHRUN and NSRUN agree with each other outside of the neutron star transition layer. This indicates that they are accreting at the same accretion rate, the fundamental scale of accretion, and we can expect the same behavior from their accretion disks. The inflowing accretion rate, \dot{M}_{in,u^r} , is a good measure to determine the mass accretion rate in the disk when most or all of the disk turbulence is averaged out, then all of the gas in the disk should have $u^r < 0$, and all of the gas in the outflow should have $u^r > 0$. This is not the case for the data we show except at small radii. For flows where the turbulence is not fully averaged out, \dot{M}_{in,u^r}

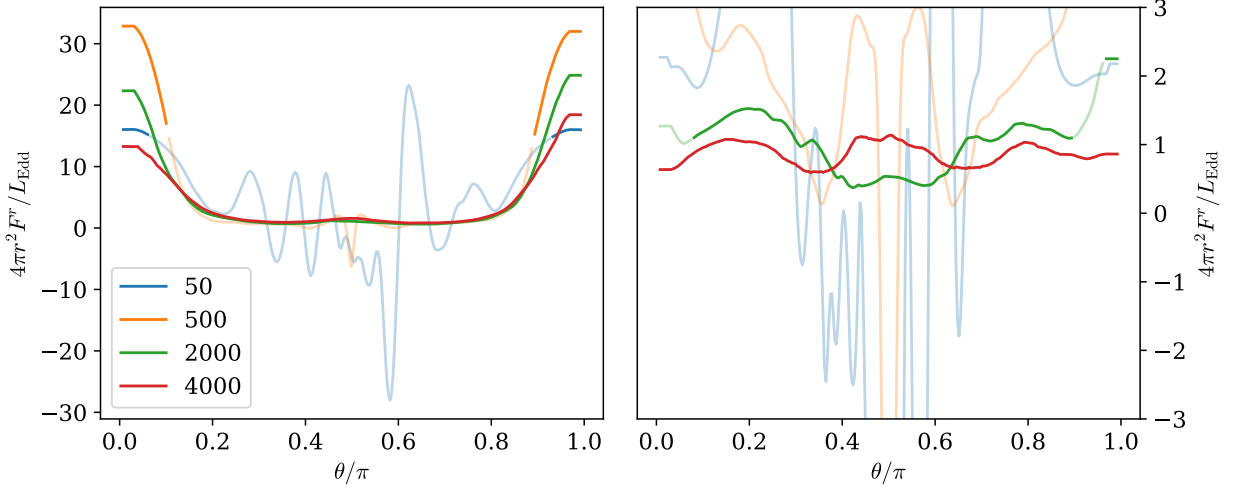


Figure 8. Here we show the radial distribution of the flux in units of the apparent isotropic luminosity, $4\pi r^2 F^r / L_{\text{Edd}}$, as a function of the line of sight for BHRUN (left) and NSRUN (right). Each line corresponds to the observable flux at a particular radius shown in the legend in units of r_g . The faded regions correspond to areas where the scattering optical depth is greater than one.

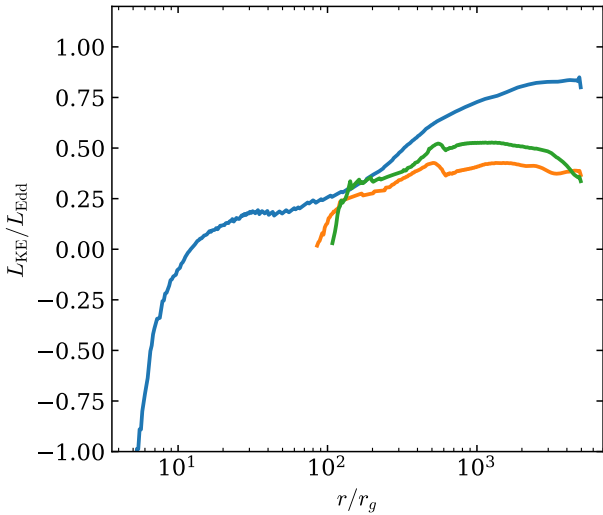


Figure 9. Here we plot the outflowing luminosity of kinetic energy L_{KE} , as a function of radius. The kinetic energy flux is integrated over the outflowing region defined by positive relativistic Bernoulli number, Be . BHRUN is shown in blue, and NSRUN is shown in orange.

is more of an upper limit. A super-Eddington accretion flow is expected to have an accretion rate that increases linearly with r (Shakura & Sunyaev 1973), and we can see from the black line, that this dependence is nearly reproduced in NSRUN. We obtain $\dot{M}_{\text{in},u^r} \propto r^{1.2}$.

We can still see a large amount of gas flowing through the NSRUN accretion disk for the t_5 interval with nearly the same slope as for t_4 , although at slightly lower values. This is likely due to the structure of the initial torus, which over very long periods of time, does not supply the accretion disk with gas at the same rate, slightly dropping with time.

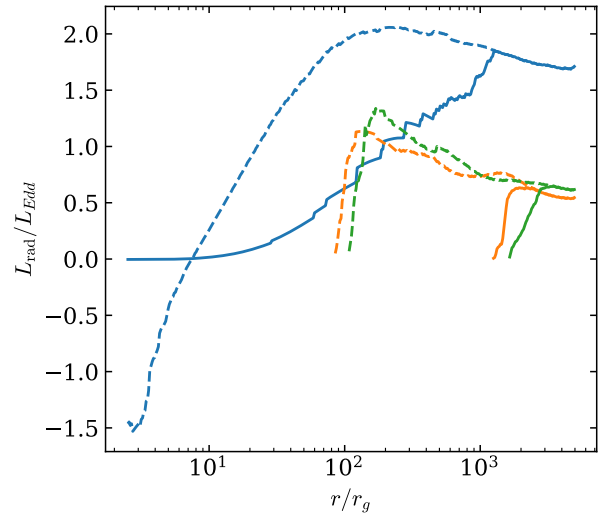


Figure 10. Radiative luminosities are shown for BHRUN (blue) and NSRUN (orange) averaged over the time period t_4 . The last time period for NSRUN, t_5 is shown in green. The solid lines correspond to the luminosity integrated over angles that are optically thin, L_{thin} , while the dashed lines show the luminosity integrated over the angles with positive Be , L_{out} .

The dashed lines correspond to the integral of the total mass flux over the regions with negative Bernoulli number,

$$\dot{M}_{\text{in},Be} = 2\pi \int_{Be < 0} -\rho u^r \sqrt{-g} d\theta,$$

Most of the gas at lower radii has negative Bernoulli number, whether or not it is part of the disk or the outflow. From Fig. 4, we can see streamlines that are initially outflowing with negative Be which turn around and return to the disk midplane, but we can also see streamlines which seem to change from negative to positive Be , and which continue to

flow outwards. It is important to note that Be is only conserved along streamlines for steady flows. Closer to the disk, the flow is very much non-steady, and so the streamlines do not always reproduce the gas trajectory. For this reason, one must be cautious when using Be as a diagnostic for outflow. It is necessary to know something about the flow, and so we put more weight on Be farther from the disk where the flow is more steady. In this way Be is more useful as a diagnostic for outflows at larger radii. We still include plots of $\dot{M}_{in,Be}$ for completeness, although they should mostly match \dot{M}_{tot} at lower radii. The departure of $\dot{M}_{in,Be}$ from \dot{M}_{in,u^r} for BHRUN is also evident from the top-left panel of Fig. 4 where there is gas which has positive Be but is directed into the black hole.

Fig. 12 shows the outflowing accretion rate, measured in the same way as the inflowing accretion rate, \dot{M}_{in,u^r} , but with opposite sign, \dot{M}_{out,u^r} . Again we show BHRUN in blue and NSRUN in orange. We also plot in green the mass outflow rate for NSRUN over the last interval, t_5 from $80\,000t_g$ to $160\,000t_g$ which was not run for the BHRUN, because it is more computationally demanding. At lower radii, \dot{M}_{out,u^r} more or less follows \dot{M}_{in,u^r} , this is because, in inflow equilibrium, the difference between them, \dot{M}_{tot} , should be constant. As the accretion rate drops with a decrease in radius, the outflow rate must also drop so that no gas can accumulate at any radius, at least for BHRUN. We have also demphasized \dot{M}_{out,u^r} at radii larger than $100r_g$, where the simulation has not reached inflow equilibrium.

For measuring the mass outflow that is expected to reach infinity, the relevant quantity is $\dot{M}_{out,Be}$, the total mass outflow rate in the positive energy region, the region which is separate from the accretion disk. These are the dashed curves in Fig. 12. $\dot{M}_{out,Be}$ is calculated in the same way as, $\dot{M}_{in,Be}$ except for $Be > 0$. In general, NSRUN shows nearly an order of magnitude larger outflow rate than BHRUN at its peak when measured over the same time period. This is why the outflows are so optically thick. The maximum outflowing accretion rate for NSRUN nearly matches \dot{M}_{in} at the edge of the transition layer. If the outflow were to converge to this value ($\sim 200L_{Edd}/c^2$) at all radii $\gtrsim 1000r_g$, then this would be a strong indication that all the inflowing matter is eventually ejected. We do not observe this however, and moreover we observe that mass is still accumulating at the inner edge. While the simulation was run for a long time, around $(160,000t_g)$, the transition layer did not seem to reach a steady state. We can see the outflow at large radii become more flat for t_5 , this also indicates that the outflow while apparently increasing with time, may slowly be approaching at least a quasi-steady state, and that outflows which are the same magnitude as the accretion rate in the disk can be expected for long periods of time.

5 DISCUSSION

We have run two long duration GRRMHD simulations, one of accretion onto a Schwarzschild black hole and one onto a neutron star (non-magnetized, non-spinning). Our black hole simulation, BHRUN, is used as a baseline to compare against the neutron star simulation for two reasons. One, it is very similar to the inflow boundary conditions used in many previous simulations. Second, it is a simple, well

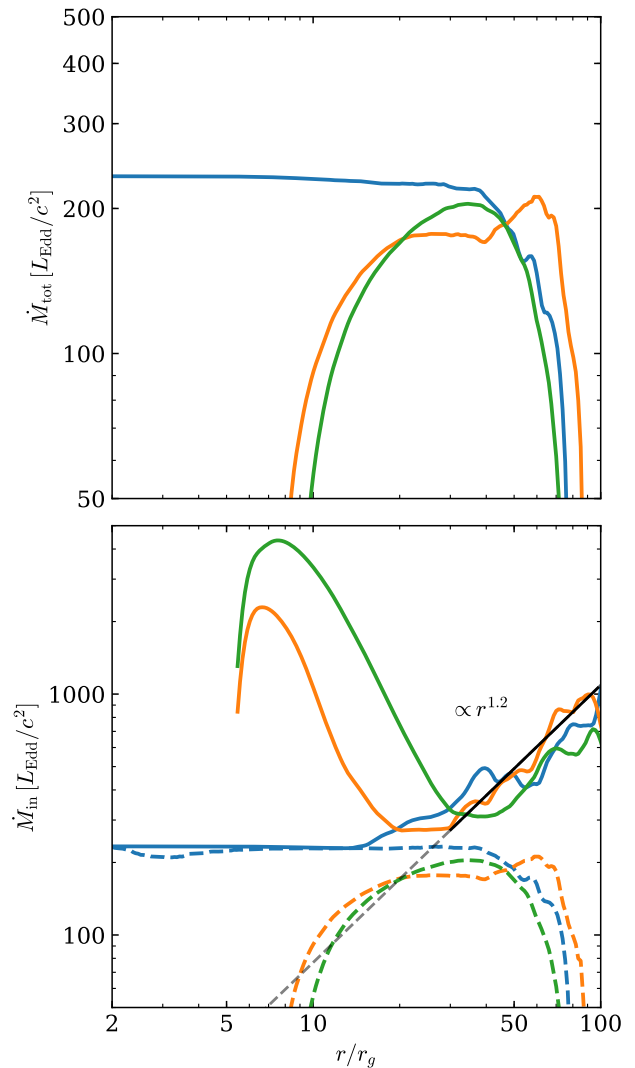


Figure 11. Top: Here we show the total accretion rate, \dot{M}_{tot} , of BHRUN (blue) and NSRUN (orange) computed from data averaged over the time interval, t_4 . In green, we show data from NSRUN time averaged over the interval t_5 . Bottom: Here we plot the mass accretion rate of the inflow, \dot{M}_{in} , again for BHRUN and NSRUN from t_4 and t_5 . We include two definitions of the inflow. The first corresponds to the solid lines which are defined as the integral over all cells with negative u^r , \dot{M}_{in,u^r} . The dashed line shows the the integral over all cells with negative Be , $\dot{M}_{in,Be}$. A power law fit to \dot{M}_{in,u^r} for NSRUN from t_4 is shown in black. The solid black line shows the radii over which the fit was performed, the dashed part is an extension of the power law for reference.

studied system, without an artificial boundary condition, and is directly comparable to other previous simulations of its type and the model more closely matches the behavior of the physical object it represents. It is immediately apparent that the simulations are quite different. The differences in the accretion disk structure are apparent inside radius $r = 30r_g$, where the flow in NSRUN begins to change into the transition layer. It is then inferred that the differences in the outflow are due to the various physical processes occurring in

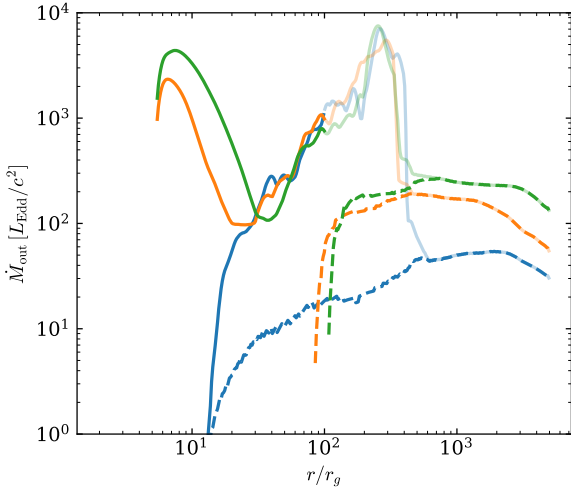


Figure 12. Here we show the outflowing mass accretion rate, \dot{M}_{out} . $\dot{M}_{\text{out},tr}$ is given by the solid lines and $\dot{M}_{\text{out},Be}$ is given by the dashed lines. Blue lines correspond to the BHRUN and orange to NSRUN both using time averaged data from the interval t_4 . The green lines shows data from NSRUN time averaged over the interval, t_5 .

the inner region of the simulation. We observed from Fig. 3 that the transition layer increases with size as time goes on.

The simulation was run for $120,000 t_g$, which only corresponds to one second of physical time, which is only one full pulsation for the pulsation periods observed in pulsating ULX systems. These observations were integrated over kilosecond time scales. The point being that even though our simulations are run for a long time (when compared to other GRRMHD simulations), they would have to be run much longer in order to capture the effects of the varying radiation source of a rotating magnetized star. Such long duration simulations are likely out of the question for 3D simulations, likely still difficult for our 2D simulations, and impossible for 2D simulations without any sort of dynamo. Nonetheless, we are free to speculate.

We observe that the radius outer boundary of the transition layer increases with a time dependence that is well described by $t^{0.85}$ power law, and we have no reason not to expect this dependence to continue until either the mass supply is quenched, the radiation pressure becomes too strong, or the central density and temperature become large enough that some other cooling mechanism becomes effective, e.g., neutrino cooling or photon cooling through outflows. The central temperature grows with a $t^{1/4}$ power law, and so neutrino cooling, which may become relevant around 10^9 K may need to be considered (depending on the central density) after a few (4-8) times the simulation length. We expect the other processes to also take much longer than a few times the current simulation time, so it would be interesting to run an even longer duration simulation, in order to study the time evolution of the outflow and luminosity as the simulation evolves. In our case, the length of our simulation was chosen so that the outflow would be causally connected to the inflow equilibrium region of the inner simulation to radii

past the photosphere. A non-physical limitation would be the transition layer growing faster than inflow equilibrium. A potential solution would be to run a black hole like simulation for long time and then to restart the simulation with an inner boundary.

Our main conclusion from our work is that the presence of a hard, nonrotating surface alone is likely not sufficient to produce enough radiation that can escape to infinity to explain the luminosities observed in ULX sources. The large amount of ejected gas not only obscures the innermost emitting regions, but also decollimates the radiation, further reducing the observed luminosity. Thus it is vital that we consider the effects of magnetic fields. This was done by [Takahashi & Ohsuga \(2017\)](#), who found a bolometric luminosity to be about an order of magnitude larger than ours, the simulation is short however, $t_{\text{stop}} = 15,000 t_g$, so more work would be required to study the effective of large amount of gas being accreted onto the magnetic field.

It would be interesting to study the case of accretion onto a non-magnetized neutron star with a different initial condition for the disk magnetic field. Our initial condition contains magnetic field loops of alternating polarity, and reconnection is allowed on a numerical level. Thus, no significant amount of magnetic flux accumulates on the inner edge of the simulation, indeed the magnetic pressure is several order of magnitude lower than the radiation pressure in the transition layer. Running a simulation with only one magnetic field loop, which normally leads to accretion in the magnetically arrested disk (MAD) state in black hole simulations ([McKinney et al. 2015](#); [Narayan et al. 2017](#)), would likely also lead to a buildup of magnetic flux in the transition layer which could be dynamically important.

One interesting application of our study could be an extension to supersoft sources (SSS) ([Long et al. 1981](#); [van den Heuvel et al. 1992](#)) and ultraluminous supersoft sources (ULS) ([Urquhart & Soria 2016](#)). ULSs are characterized by peak temperatures of around 10^6 K, with bolometric luminosities at a few times 10^{39} erg s^{-1} and photospheres at radii of around 10^4 km. SSSs are classified similarly with lower temperatures ($\sim 10^5$ K, $\sim 10^6$ K) and luminosities ($\sim 10^{36}$ erg s^{-1} , $\sim 10^{38}$ erg s^{-1}). The effective temperature of NSRUN can be computed by measuring the radiative energy density around the photosphere which is on average around a few times 10^6 K. The radius of the photosphere is around 5000 km. These features are indicative of ULS sources, although the bolometric luminosity is about an order of magnitude too low, closer to the higher end for SSSs. While SSSs can be well explained by nuclear burning on the surface of a white dwarf ([van den Heuvel et al. 1992](#)), ULSs, like ULXs have been harder to model. It would be interesting in future work to do post-processing of NSRUN to generate spectra to see if they match any of the more specific characteristics of ULSs or SSSs.

5.1 Comparison to [Takahashi et al. \(2018\)](#)

After this work was completed we became aware of an important publication by [Takahashi et al. \(2018\)](#) (TMO18), who obtained similar results to ours by running a shorter simulation ($7000 t_g$), demonstrating the feasibility of super-Eddington accretion onto a non-magnetized neutron star. It is vital that we make a comparison to the work by TMO18,

as the simulations they have run should be directly comparable to ours. TMO18 have performed two simulations, one onto a black hole, and one onto a reflective inner boundary as in our work. Both codes are GRRMHD solvers with M_1 closure. The code used is the same as used by the authors in their previous work. Both our simulations and those of TMO18 show a power law behavior at the inner edge of the simulation. TMO18 report a significant increase in the rate of ejected mass over their black hole simulation. Indeed we also infer a roughly ten times increase in the mass outflow rate for NSRUN over BHRUN. The authors also report an increase in the radius of the photosphere over the black hole case. We find a much larger increase in the photosphere however, reaching out to a couple thousand r_g . This is likely due to the length of our simulations, which are run for more than ten times the length of the simulations in TMO18, and so we believe we are able to make a more accurate statement about the mass outflow to larger radii, and about the radiative luminosity, which TMO18 does not address.

One interesting difference is found in the strong change in the angular velocity in the transition layer, seen in our simulations. TMO18 show the centripetal force, which can be used as a proxy for Ω (indeed, in the Newtonian case it is proportional to Ω^2). TMO18 show that the centripetal force transitions from super-Keplerian to about half Keplerian. This contrasts against our simulations where Ω transitions to practically zero at the inner edge of the simulation, even at early times. This difference could be due to differences in the inner boundary condition for u^ϕ . When we average our data over the same time interval as is described in TMO18 (3000-5000 t_g) and we examine Ω/Ω_K we see that it transitions from unity at about 10 r_g to 0.3 at the stellar surface ($5r_g$). This corresponds to the same range of radii over which the centripetal force of TMO18 transitions to about 0.6 times the Keplerian value which would indicate an $\Omega/\Omega_K \approx 0.8$, more than twice the angular velocity ratio of our simulation. This indicates that we have a stronger torque at the inner edge of our simulation, and so it is probably easier for gas to accumulate in the transition layer. It will be beneficial in the future to study angular momentum transfer through the inner boundary for different boundary conditions.

5.2 Caveats

It is important to stress that our simulations are a first attempt at measuring the effects of a hard surface in the context of a global, radiative, MRI-driven, super-Eddington accretion flow. More physics is planned in future implementations. Indeed there are a number of issues that must be addressed before we may consider these results truly robust.

First, our simulations are performed in 2D axisymmetry. [Sądowski & Narayan \(2016\)](#) has shown that non-axisymmetric effects can lead to a lower luminosity accretion flow around a black hole. Since the luminosities we measured were on the low end of what is expected for ULX objects, we cannot be sure if a three dimensional simulation would be bright enough. It is possible that this difference would not occur in the presence of hard surface, but a fully three dimensional simulation would be required to confirm.

Second, we have neglected the effects of rotation. Accretion onto a rapidly rotating star will release less energy than accretion onto a stationary star. The gas will also be

less bound however. For a one second rotational period, the effects of rotation at the neutron star surface should be negligible; however, the acceleration of gravity scales as r^{-2} while centripetal acceleration increases with r . At larger radii, this may become relevant if the accreted atmosphere rotates nearly uniformly.

6 SUMMARY

We have found that a reflective, non-rotating boundary at the inner edge of an accretion disk simulation has a significant effect on the behavior and structure of the inner disk as well as its emission and outflows. We observe large amounts of gas accumulating on the inner boundary in a transition layer, where the angular velocity transitions from its Keplerian value to near zero. We also found lower rates in the outflow of kinetic energy over the black hole case. However, we did measure larger mass outflow rates, affecting the release of radiation to the observer. In fact, the hard surface of a non-magnetized neutron star leads to lower radiative luminosities in super-Eddington flows relative to black holes, and with radiation decollimated to the point where they are not likely to explain even the lowest luminosity ULXs, although they may be applicable to ULXs or SSSs. This work is a first step in a larger plan to study accretion processes around a neutron star. Further work includes studying different accretion rates, including rotation, and eventually the addition of stellar magnetic fields.

ACKNOWLEDGEMENTS

The first author thanks Ramesh Narayan, Maciek Wielgus, and Jean-Pierre Lasota for advice and illuminating conversations. Research supported in part by the Polish NCN grants 2013/08/A/ST9/00795 and 2017/27/N/ST9/00992. Computations in this work were performed on the Prometheus machine, part of the PLGrid infrastructure.

REFERENCES

- Alme M. L., Wilson J. R., 1973, *ApJ*, **186**, 1015
- Bachetti M., et al., 2014, *Nature*, **514**, 202
- Balbus S. A., Hawley J. F., 1991, *ApJ*, **376**, 214
- Basko M. M., Sunyaev R. A., 1976, *MNRAS*, **175**, 395
- Bradshaw C. F., Fomalont E. B., Geldzahler B. J., 1999, *ApJ*, **512**, L121
- Chamel N., Haensel P., 2008, *Living Reviews in Relativity*, **11**, 10
- Colbert E. J. M., Mushotzky R. F., 1999, *ApJ*, **519**, 89
- Dhang P., Sharma P., Mukhopadhyay B., 2016, *MNRAS*, **461**, 2426
- Ekşi K. Y., Andaç İ. C., Çıkmıtoğlu S., Gençali A. A., Güngör C., Öztekin F., 2015, *MNRAS*, **448**, L40
- El Mellah I., Casse F., 2015, *MNRAS*, **454**, 2657
- Fiacconi D., Pinto C., Walton D. J., Fabian A. C., 2017, *MNRAS*, **469**, L99
- Fürst F., et al., 2016, *ApJ*, **831**, L14
- Gammie C. F., McKinney J. C., Tóth G., 2003, *ApJ*, **589**, 444
- Hashizume K., Ohsuga K., Kawashima T., Tanaka M., 2015, *Publications of the Astronomical Society of Japan*, **67**, 58
- Inogamov N. A., Sunyaev R. A., 1999, *Astronomy Letters*, **25**, 269
- Israel G. L., et al., 2017a, *Science*, **355**, 817

- Israel G. L., et al., 2017b, *MNRAS*, **466**, L48
- Jiang Y.-F., Stone J. M., Davis S. W., 2014, *ApJ*, **796**, 106
- Kawashima T., Mineshige S., Ohsuga K., Ogawa T., 2016, *PASJ*, **68**, 83
- King A. R., Davies M. B., Ward M. J., Fabbiano G., Elvis M., 2001, *ApJ*, **552**, L109
- King A., Lasota J.-P., Kluźniak W., 2017, *MNRAS*, **468**, L59
- Kluźniak W., Lasota J.-P., 2015, *MNRAS*, **448**, L43
- Kluźniak W., Wagoner R. V., 1985, *ApJ*, **297**, 548
- Kluźniak W., Wilson J. R., 1991, *ApJ*, **372**, L87
- Koliopanos F., Vasilopoulos G., Godet O., Bachetti M., Webb N. A., Barret D., 2017, *A&A*, **608**, A47
- Komissarov S. S., 1999, *MNRAS*, **303**, 343
- Long K. S., Helfand D. J., Grabelsky D. A., 1981, *ApJ*, **248**, 925
- McKinney J. C., Dai L., Avara M. J., 2015, *MNRAS*, **454**, L6
- Mukhopadhyay B., Fang L. Z., 2002, *International Journal of Modern Physics D*, **11**, 1305
- Mushtukov A. A., Suleimanov V. F., Tsygankov S. S., Poutanen J., 2015a, *MNRAS*, **447**, 1847
- Mushtukov A. A., Suleimanov V. F., Tsygankov S. S., Poutanen J., 2015b, *MNRAS*, **454**, 2539
- Mushtukov A. A., Suleimanov V. F., Tsygankov S. S., Ingram A., 2017, *Monthly Notices of the Royal Astronomical Society*, **467**, 1202
- Mushtukov A. A., Verhagen P. A., Tsygankov S. S., van der Klis M., Lutovinov A. A., Larchenkova T. I., 2018, *MNRAS*, **474**, 5425
- Narayan R., Yi I., 1995, *ApJ*, **452**, 710
- Narayan R., Garcia M. R., McClintock J. E., 1997, *ApJ*, **478**, L79
- Narayan R., Sądowski A., Penna R. F., Kulkarni A. K., 2012, *MNRAS*, **426**, 3241
- Narayan R., Sądowski A., Soria R., 2017, *MNRAS*, **469**, 2997
- Ogawa T., Mineshige S., Kawashima T., Ohsuga K., Hashizume K., 2017, *PASJ*, **69**, 33
- Ohsuga K., Mori M., Nakamoto T., Mineshige S., 2005, *ApJ*, **628**, 368
- Parfrey K., Tchekhovskoy A., 2017, *ApJ*, **851**, L34
- Penna R. F., Kulkarni A., Narayan R., 2013, *A&A*, **559**, A116
- Pintore F., Zampieri L., Stella L., Wolter A., Mereghetti S., Israel G. L., 2017, *ApJ*, **836**, 113
- Popham R., Sunyaev R., 2001, *ApJ*, **547**, 355
- Revnivtsev M., Mereghetti S., 2015, *Space Sci. Rev.*, **191**, 293
- Romanova M. M., Ustyugova G. V., Koldoba A. V., Lovelace R. V. E., 2012, *MNRAS*, **421**, 63
- Sądowski A., Narayan R., 2015, *MNRAS*, **454**, 2372
- Sądowski A., Narayan R., 2016, *MNRAS*, **456**, 3929
- Sądowski A., Narayan R., Tchekhovskoy A., Zhu Y., 2013, *MNRAS*, **429**, 3533
- Sądowski A., Narayan R., Tchekhovskoy A., Abarca D., Zhu Y., McKinney J. C., 2015, *MNRAS*, **447**, 49
- Shakura N. I., Sunyaev R. A., 1973, *A&A*, **24**, 337
- Shklovsky I. S., 1967, *ApJ*, **148**, L1
- Sibgatullin N. R., Sunyaev R. A., 2000, *Astronomy Letters*, **26**, 772
- Sunyaev R. A., Shakura N. I., 1986, *Soviet Astronomy Letters*, **12**, 117
- Takahashi H. R., Ohsuga K., 2017, *ApJ*, **845**, L9
- Takahashi H. R., Mineshige S., Ohsuga K., 2018, *ApJ*, **853**, 45
- Toropina O. D., Romanova M. M., Lovelace R. V. E., 2012, *MNRAS*, **420**, 810
- Urquhart R., Soria R., 2016, *MNRAS*, **456**, 1859
- Walton D. J., et al., 2018, *MNRAS*, **473**, 4360
- Wiktorowicz G., Sobolewska M., Lasota J.-P., Belczynski K., 2017, *ApJ*, **846**, 17
- Yang X.-H., Yuan F., Ohsuga K., Bu D.-F., 2014, *ApJ*, **780**, 79
- Čemeljić M., Shang H., Chiang T.-Y., 2013, *ApJ*, **768**, 5
- van den Heuvel E. P. J., Bhattacharya D., Nomoto K., Rappaport S. A., 1992, *A&A*, **262**, 97

This paper has been typeset from a $\text{\TeX}/\text{\LaTeX}$ file prepared by the author.